RESEARCH ARTICLE

Stabilizing oxygen by high-valance element doping for high-performance Li-rich layered oxides

Errui Wang[1,2,3] | Dongdong Xiao[4] | Tianhao Wu[1,2] | Boya Wang[1,2] | Yinzhong Wang[1,2] | Lingqiao Wu[1,2] | Xu Zhang[1,2] | Haijun Yu[1,2]

[1]Institute of Advanced Battery Materials and Devices, Faculty of Materials and Manufacturing, Beijing University of Technology, Beijing, China

[2]Key Laboratory of Advanced Functional Materials, Ministry of Education, Beijing University of Technology, Beijing, China

[3]College of Chemistry and Material Engineering, Anhui Science and Technology University, Bengbu, China

[4]Beijing National Laboratory for Condensed Matter Physics, Institute of Physics, Chinese Academy of Sciences, Beijing, China

Correspondence
Dongdong Xiao, Beijing National Laboratory for Condensed Matter Physics, Institute of Physics, Chinese Academy of Sciences, Beijing 100190, China.
Email: dongdongxiao@iphy.ac.cn

Haijun Yu, Institute of Advanced Battery Materials and Devices, Faculty of Materials and Manufacturing, Beijing University of Technology, Beijing 100124, China; Key Laboratory of Advanced Functional Materials, Ministry of Education, Beijing University of Technology, Beijing 100124, China
Email: hj-yu@bjut.edu.cn

Abstract

Lithium-rich layered oxides (LLOs) with high energy density and low cost are regarded as promising candidates for the next-generation cathode materials for lithium-ion batteries (LIBs). However, there are still some drawbacks of LLOs such as oxygen instability and irreversible structure reconstruction, which seriously limit their electrochemical performance and practical applications. Herein, the high-valence Ta doping is proposed to adjust the electronic structures of transition metals, which form strong Ta-O bonds and reduce the covalency of Ni-O bonds, thereby stabilizing the lattice oxygen and enhancing the structural/thermal stabilities of LLOs during electrochemical cycling. As a result, the optimized Ta-doped LLO can deliver a capacity retention of 80% and voltage decay of 0.34 mV cycle^{-1} after 650 cycles at 1C. This study enriches the fundamental understanding of the electronic structure adjustment of LLOs and contributes to the optimization of LLOs for high-energy LIBs.

KEYWORDS
elemental doping, lithium-ion battery, lithium-rich layered oxides, oxygen release, voltage decay

1 | INTRODUCTION

To date, the rapidly increasing demand for high-energy lithium-ion batteries (LIBs) for electric vehicles and energy-storage systems calls for the development of high-energy-density and highly stable cathode materials.[1–3] Traditional cathode materials based on the transition metal (TM) cationic redox usually deliver limited capacities, which can hardly fulfill the high-energy demand of LIBs.[2,4] Therefore, lithium-rich layered oxides (LLOs, $xLi_2MnO_3 \cdot (1-x)LiTMO_2$ (TM = Mn, Ni, Co, or other metals)) with high specific capacities and energy densities become a promising candidate for the next-generation cathode materials.[5,6] Different from traditional cathode materials, LLOs deliver capacities from not only the TM redox (e.g., $Ni^{2+/4+}$, $Co^{3+/4+}$, etc.), but also the O redox ($O^{2-}/O^{\alpha-}$, $\alpha < 2$).[7–9]

However, LLOs still suffer from diverse drawbacks such as rapid capacity and voltage decay, which are rooted in their intrinsic structures. It has been demonstrated that LLOs are comprised of $LiTMO_2$ and Li_2MnO_3 crystal domains.[10,11] The Li_2MnO_3 crystal domain can be activated at high cut-off voltages (>4.4 V vs. Li^+/Li), triggering the oxygen anionic redox as well as the irreversible oxygen loss, which promotes the migration of TMs and irreversible structure transformation of LLOs.[5,12,13] As a result, LLOs often show rapid capacity fading and voltage decay, which seriously obstructs their practical applications.[14–16] In addition, thermal stability is also important for the safety of LIBs, which is still far from satisfying for LLOs.[5,17]

To overcome these issues, a variety of strategies have been developed over the past years, including component design,[12,18,19] lattice/surface elemental doping,[1,20–22] surface modification,[23–25] structural design,[26] combined strategies,[27,28] and binder/electrolyte engineering.[29–31] Among them, bulk doping is facile and effective to tailor the properties of lattice oxygen and suppress the irreversible structure transformations.[22,32–34] It is of primary importance to clarify the effects of diverse element dopants in LLOs for tailoring their functions. One of the most effective strategies is enhancing the strength of TM-O bonds, which can stabilize the lattice O and TM against element loss and structure degradation.[35] Toward this goal, heavy ions (Zr^{4+}, Ti^{4+}, Nb^{5+}, W^{6+}, etc.) can be employed to form stronger bonds with oxygen than those of Ni-O, Co-O, and Mn-O, which have been shown to be effective for the optimization of LLOs.[32,36,37] On the other hand, as a typical high-valance dopant, Ta^{5+} has been demonstrated to improve the electrochemical performance of Ni-rich cathode materials.[37–39] However, the effects of Ta doping on the structures and electrochemical performance of LLOs are still not clear,

requiring further studies to enrich the fundamental understanding of the doping effect and enhance the performance of high-energy LIBs.

In this study, a bulk Ta doping strategy is proposed to greatly improve the long-cycle performance and thermal stability of LLOs. By combining various characterizations including X-ray absorption spectroscopy (XAS), in situ differential electrochemical mass spectrometry (DEMS), in situ X-ray diffraction (XRD), differential scanning calorimetry (DSC), and first-principles calculations, the effects of Ta on the structure and electrochemistry of LLOs are well elucidated. It is found that Ta doping can adjust the electronic structures of TMs by forming strong Ta-O bonds and reducing the covalency of Ni-O bonds, which can stabilize the lattice oxygen and enhance the structural/thermal stabilities of LLOs for long cycles.

2 | EXPERIMENTAL SECTION

2.1 | Material preparation

The synthesis of $Mn_{0.59}Ni_{0.29}Co_{0.12}CO_3$ (TMCO$_3$) precursor and pristine $Li_{1.13}Mn_{0.517}Ni_{0.256}Co_{0.097}O_2$ (LLO) was according to our previously reported co-precipitation method.[1,5]

To prepare the Ta-doped LLOs ($Li_{1.13}[Mn_{0.594}Ni_{0.294}Co_{0.112}]_{0.87-x} Ta_xO_2$ [$x = 0.005$, 0.01, and 0.02]) with 0.5 mol% Ta (LLO-0.5), 1 mol% Ta (LLO-1), and 2 mol% Ta (LLO-2), 20 g TMCO$_3$ was uniformly dispersed in 80 ml ethanol, followed by adding ethanol tantalum ($C_{10}H_{25}O_5Ta$) with the designed amount for each. Then, the suspension was heated at 80°C in an oil bath with continuous stirring for 8 h. The treated TMCO$_3$ was collected by filtering three times with ethanol washing. Eventually, the collected TMCO$_3$ was sintered at 500°C for 5 h and then sintered at 850°C for 12 h under an air atmosphere with 1% excess Li_2CO_3 to yield the final doped materials.

2.2 | Material characterization

The morphologies of LLO and Ta-doped LLOs were examined by field-emission scanning electron microscopy (FEI-SEM, SU80020). The crystal structures of LLOs were analyzed using powder XRD (Bruker D8 Advance, Cu-Kα radiation ($\lambda = 1.5405$ Å)) with a scan range of 2θ from 10° to 125°. The XRD profiles were refined with Rietveld refinement using the TOPAS software. The average chemical compositions of LLO and LLO-1 were measured with inductively coupled plasma (ICP) spectroscopy (OPTIMA7000DV). Atomic structures of LLOs

were characterized using atomic-resolution high-angle annular dark field (HAADF) and annular bright field (ABF) scanning transmission electron microscopy (STEM) imaging on an aberration-corrected JEOL-ARM200CF electron microscope. And element distributions of LLOs were mapped using a JEOL-F200 electron microscope with double energy dispersive X-ray detectors. Electronic structures were monitored by soft X-ray absorption spectroscopy (sXAS, beamline MCD-A, and MCD-B at National Synchrotron Radiation Laboratory [NSRL] in total electron yield [TEY] mode, Hefei, China) and X-ray photoelectron spectroscopy (XPS, PHI Quanteral II, Japan). The DSC measurements of the 4.8 V-charged LLO and LLO-1 electrodes were conducted on a DSC analyzer (NETZSCH STA 449F3, Germany), with a ramping rate of 3°C min^{-1} from 25°C to 350°C under Ar flow. In situ DEMS (Hiden Analytical, HPR-20, R&D) was carried out to detect the O_2 and CO_2 releases of LLO and LLO-1 during the initial charge/discharge process from 2 to 4.8 V at 25°C. Gas detecting was started at least 1 h earlier than the start of battery charging to ensure the reliable measurement of the baseline. Volatile molecules with a molecular mass of 32 (O_2) and 44 (CO_2) were set to be monitored online. In the in situ DEMS study, the loading masses of LLO and LLO-1 in the working electrodes are $7.5 \pm 0.2 \, mg/cm^2$, and the corresponding charge/discharge current density is 74 mA g^{-1}.

2.3 | DFT calculations

All computed energies are obtained using the Vienna ab initio Simulation Package (VASP) using the projector-augmented wave (PAW) method. The Brillouin zone was adopted with a $2 \times 2 \times 2$ Γ-centered k-mesh, and the plane-wave basis is cut off by 520 eV. Atomic geometries are converged to a maximum force tolerance of 0.02 eV/Å, the total energy converged was set to be 10^{-5} eV.

2.4 | Electrochemical measurements

The working electrodes were fabricated by mixing the as-prepared cathode materials (80 wt%), carbon black (10 wt%), and PVDF (10 wt%) binder in *N*-methyl pyrrolidinone (NMP). Then, the slurry mixture was spread uniformly on an aluminum foil current collector with a typical loading amount of 3.5–4.0 mg cm^{-2} and dried at 100°C overnight. The electrochemical performances of the cathodes were examined in CR2032 coin cells, coupled with Li foil as the counter electrode, Celgard 2400 as the separator, and 1 M LiPF$_6$ and 1% lithium difluoro(oxalato)borate (LiDFOB) in a mixture of

ethylene carbonate (EC)/dimethyl carbonate (DEC) (1/1 by volume) as the electrolyte. The galvanostatic cycling was conducted in the voltage range of 2.0 and 4.8 V for the initial cycle at 0.1 C (1C = 200 mA g^{-1}) and then between 2.0 and 4.6 V for the following cycles at 1C.

3 | RESULTS AND DISCUSSION

The morphologies of LLO and Ta-doped LLOs were characterized by scanning electron microscopy (SEM). As shown in Figure 1A–D, all cathode materials appear as spherically shaped secondary particles. Compared with that of LLO, the surfaces of Ta-doped LLOs are smoother. As shown in the high-resolution SEM images in Supporting Information: Figure S1, the morphologies and sizes of the primary particles in the pristine and Ta-doped LLOs are similar, suggesting that Ta doping has a minor influence on the growth of primary particles. On the other hand, Ta doping can reduce the porosity of secondary particles. The specific surface areas of LLO, LLO-0.5, LLO-1, and LLO-2 are 6.420, 5.015, 3.818, and 3.359 m^2 g^{-1}, respectively. It means that Ta doping can optimize the contact between primary particles. Therefore, Ta-doped LLOs may reduce the contact area with electrolytes, thereby inhibiting the interfacial side reactions and improving the cycling performance of LLOs.[5] Energy dispersive X-ray spectroscopy (EDS) was employed to evaluate the element distributions of LLO and Ta-doped LLOs (Supporting Information: Figure S2). The elemental maps demonstrate the homogenous distributions of Ta, Mn, Co, and Ni, which indicates that Ta was doped homogenously in LLOs. Moreover, the chemical compositions of Ta-doped LLOs were examined by ICP (Supporting Information: Table S1), which are very close to the designed compositions.

To elucidate the atomic structures of LLO and Ta-doped LLOs, LLO, and LLO-1 were selected as representative materials for the investigation by the atomic resolution high-angle annular dark-field scanning transmission electron microscopy (HAADF-STEM), as shown in Figure 1E,F. There are no obvious bright spots in the Li slabs, indicating that LLO and LLO-1 have well-defined layered structures. The fast Fourier transformation (FFT) patterns are provided in the insets of Figure 1E,F, showing the maintenance of the layered structure of LLOs after Ta doping.[10,11] The interplanar spacing of LLO is 4.69 Å, corresponding to the spacing of the (003) plane of the LiTMO$_2$ crystal domain or that of the (001) plane of the Li$_2$MnO$_3$ crystal domain. In LLO-1, the interplanar spacing is expanded to 4.74 Å, which may be attributed to the larger radius of Ta^{5+} (0.64 Å) than that of Mn^{4+} (0.53 Å). Moreover, the nanometer-resolution
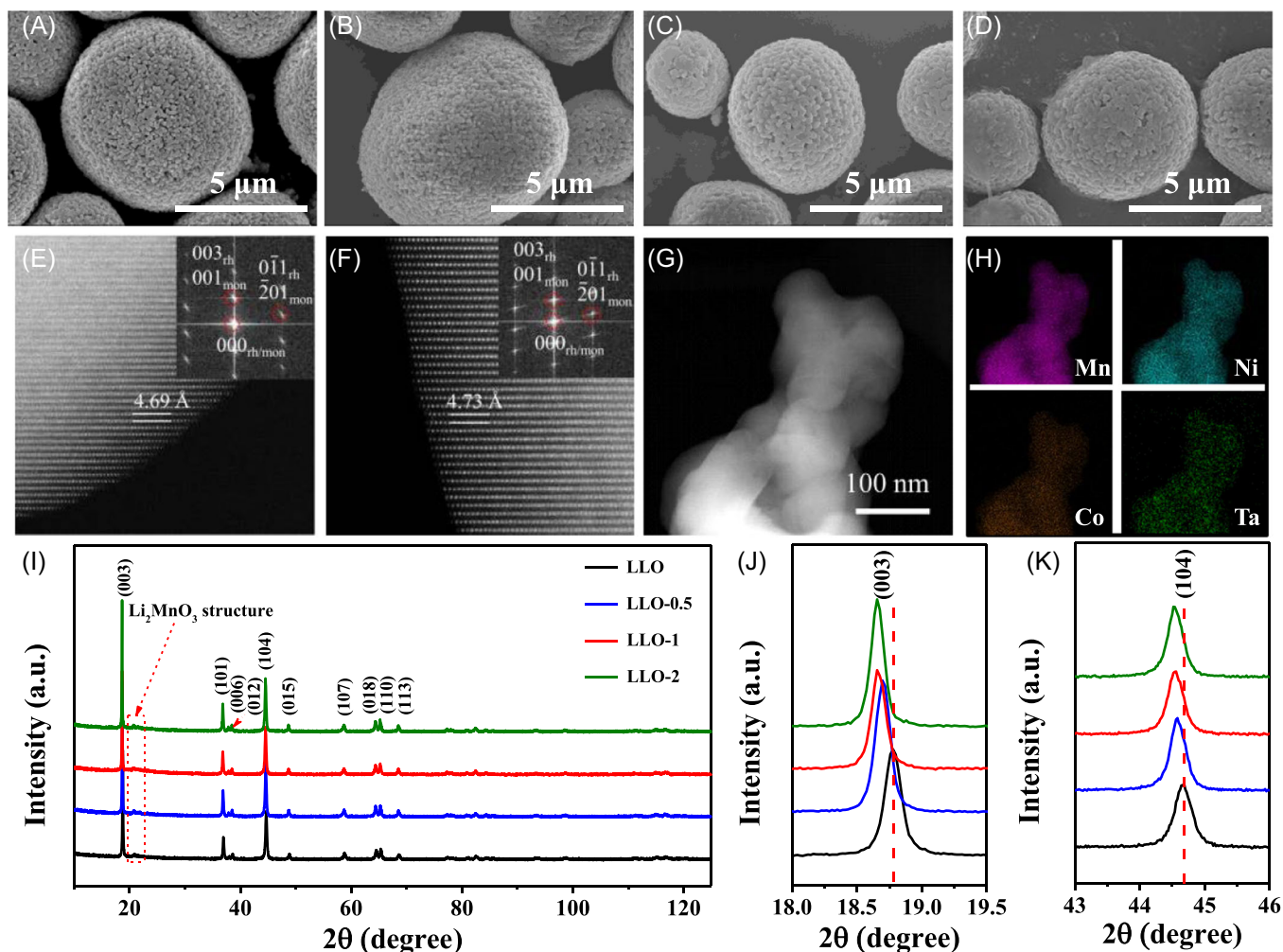
FIGURE 1 (A–D) SEM images of lithium-rich layered oxides (LLOs) (A), LLO-0.5 (B), LLO-1 (C), and LLO-2 (D). (E, F) Atomic-resolution HAADF-STEM images of LLO (E) and LLO-1 (F). The corresponding fast Fourier transformation (FFT) patterns were shown as insets, two sets of patterns originated from the $LiTMO_2$ crystal domain along the $[100]_{rh}$ crystallographic direction and Li_2MnO_3 crystal domain along the $[010]_{mon}$ crystallographic directions (G, H) HAADF-STEM image of LLO-1 (G) and corresponding elemental distributions from STEM-EDX maps (H). (I) X-ray powder diffraction (XRD) patterns of all LLOs. (J, K) The enlarged views of (003) (J) and (104) (K) peaks of XRD patterns from (I).

STEM-EDX maps of LLO-1 fragments in Figure 1H obviously indicate the highly uniform distributions of Mn, Ni, Co, and Ta elements in the bulk. To further evaluate the doping uniformity of Ta in the bulk LLO-1, a typical SEM image of the cross-section of LLO-1 and corresponding EDS line analyses of Ta along the arrow in the cross-section SEM image (Supporting Information: Figure S3A,B). Obviously, the concentrations of Ni, Co, Mn, and Ta keep almost constant from the surface to the center of the secondary particle, indicating that Ta has been uniformly doped into the bulk LLO-1 during high-temperature calcination.

X-ray powder diffraction (XRD) was further employed to study the influence of Ta doping on the crystal structures of LLOs. Figure 1I shows the XRD patterns of all LLOs.[20,40,41] Meanwhile, the obvious separations of (006)/(102) and (108)/(110) peaks demonstrate the featured

layered structure of all materials. Compared with that of LLO, the (003) peak of Ta-doped LLOs shifts to lower angles upon the increase of Ta doping amount, indicating that Ta doping can expand the interlayer spacing,[42] in consistency with the HAADF-STEM result. Moreover, the (104) peak shows a similar trend, implying the increase of parameter a, which is likely owing to the large size of Ta^{5+} ions. To explore the detailed structural information (lattice parameters a, c, and unit cell volume V), the XRD patterns were analyzed by structure refinement, as shown in Supporting Information: Figure S4 and Table S2. Compared with those of LLO, the increased tendencies of c and V of Ta-doped LLOs with the increase of Ta doping amount may be attributed to the larger radius of Ta^{5+} than that of Mn^{4+}.

To investigate the influence of Ta doping on the electronic structures of TM and O in LLOs, XPS spectra
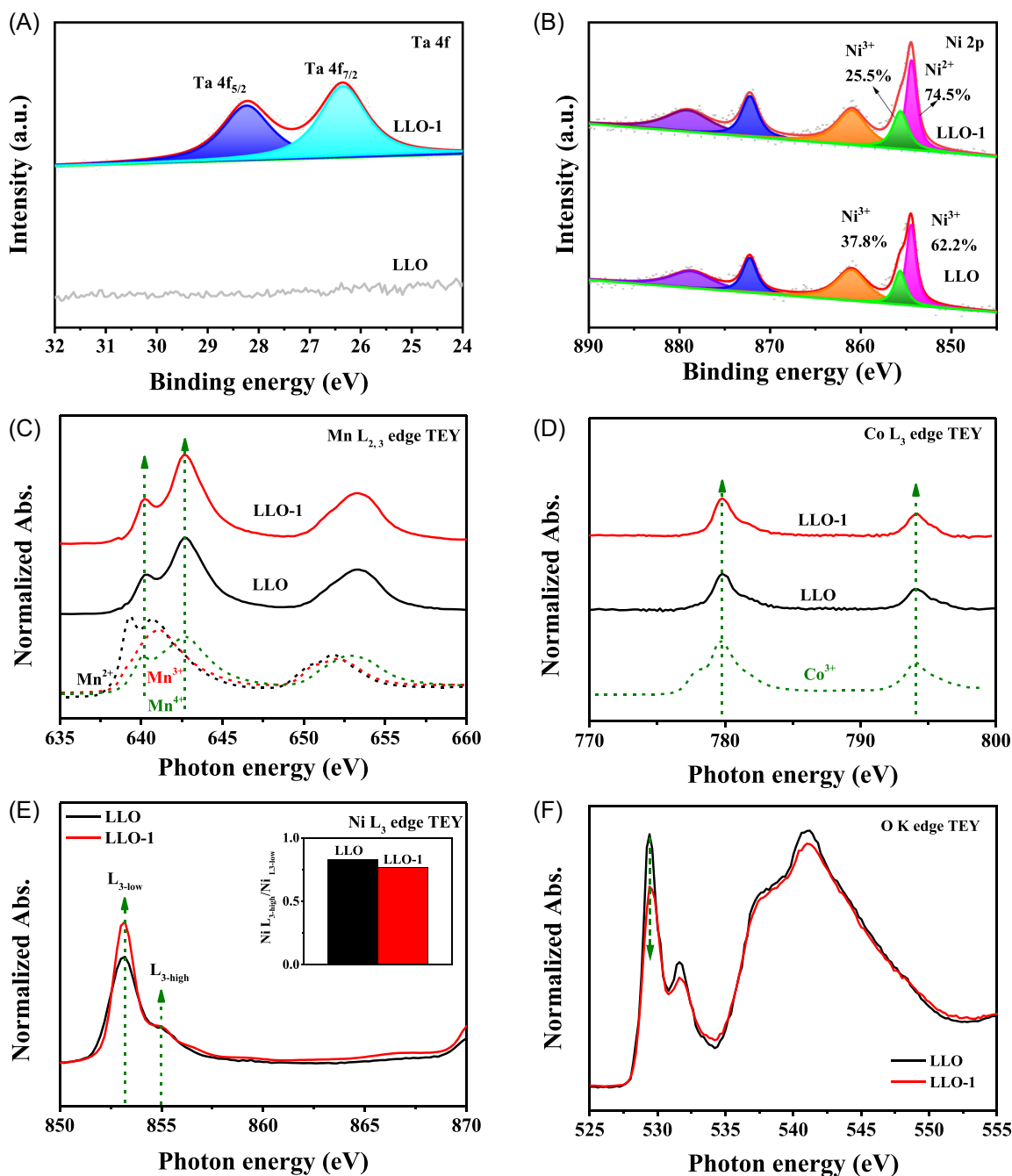
FIGURE 2 (A, B) X-ray photoelectron spectroscopy (XPS) Ta 4f (A) and Ni 2p (B) spectra of lithium-rich layered oxides (LLOs) and LLO-1. (C–F) Mn L-edge (C), Co L-edge (D), Ni L-edge (E), and O K-edge (F) X-ray adsorption spectroscopy (sXAS) spectra of LLO and LLO-1 in the total electron yield (TEY) mode.

of LLO and LLO-1 were acquired as shown in Figures 2A,B, and Supporting Information: Figure S5. As shown in Figure 2A, compared with LLO, the Ta-doped LLO-1 displays two new peaks located at 26.3 and 28.2 eV, which can be assigned to Ta $4f_{5/2}$ and Ta $4f_{7/2}$, respectively.[5,43] Moreover, after Ta doping, there are no significant shifts for the characteristic spectra of Mn 2p and Co 2p (Supporting Information: Figure S5), while the Ni 2p peak shifts to the lower binding energy

(Figure 2B), indicating that Ta doping mainly affects the valence of Ni rather than those of Co and Mn.

sXAS was also used to study LLO and LLO-1, which further reveals the influence of Ta doping on the elemental valence state. The normalized Mn $L_{2,3}$, and Co L_3-edge results in the TEY mode are shown in Figure 2C,D, respectively. No significant peak shifts after Ta doping could be observed, suggesting no change in the elemental valence states of Mn and Co. Figure 2D shows

the obviously increased intensity of the $L_{3\text{-low}}$ peak in the Ni L_3-edge spectrum. The relative intensity of $L_{3\text{-low}}$ and $L_{3\text{-high}}$ peaks ($L_{3\text{-high}}/L_{3\text{-low}}$) can provide general information about the valence changes of Ni. A higher $L_{3\text{-high}}/L_{3\text{-low}}$ indicates a higher Ni oxidation state.[44,45] The calculated $L_{3\text{-high}}/L_{3\text{-low}}$ results of all LLOs are shown in the inset of Figure 2E, suggesting that $L_{3\text{-high}}/L_{3\text{-low}}$ is decreased upon Ta doping. This result illustrates that the valence of Ni is partially reduced with Ta doping, which can be ascribed to the high-valence Ta^{5+} induced rebalance of charge.[37] Figure 2F shows the O K-edge spectra of LLO and LLO-1 in the TEY mode. The pre-edge peak at ~529.5 eV corresponds to the transfer of O 1s electrons to the hybridized state of the TM3d and O2p orbitals. The intensity of the pre-edge peak of LLO-1 is reduced compared with that of LLO, which can be attributed to the change in the local electronic structure of O atoms and the reduced covalency of the TM-O bond.[46] Based on the above discussion, the decreased intensity of the pre-edge peak in the O K-edge spectra of LLO-1 is mainly attributed to the reduced covalency of the Ni-O bond after Ta doping. The reduction of the Ni-O covalency is beneficial to the cycle stability of LLOs due to more stable lattice O at high voltages.[22]

Figure 3A shows the charge/discharge curves of LLO and Ta-doped LLOs in the first cycle at 0.1C (1C = 200 mAh g^{-1}) and 25°C between 2.0 and 4.8 V. In the charge process, the four LLOs deliver similar charge capacities in the voltage slope region (<4.4 V), while the Ta-doped LLOs deliver gradually reduced charge capacities with the increase of Ta amount in the voltage plateau region (>4.4 V). It indicates that the Ta doping does not
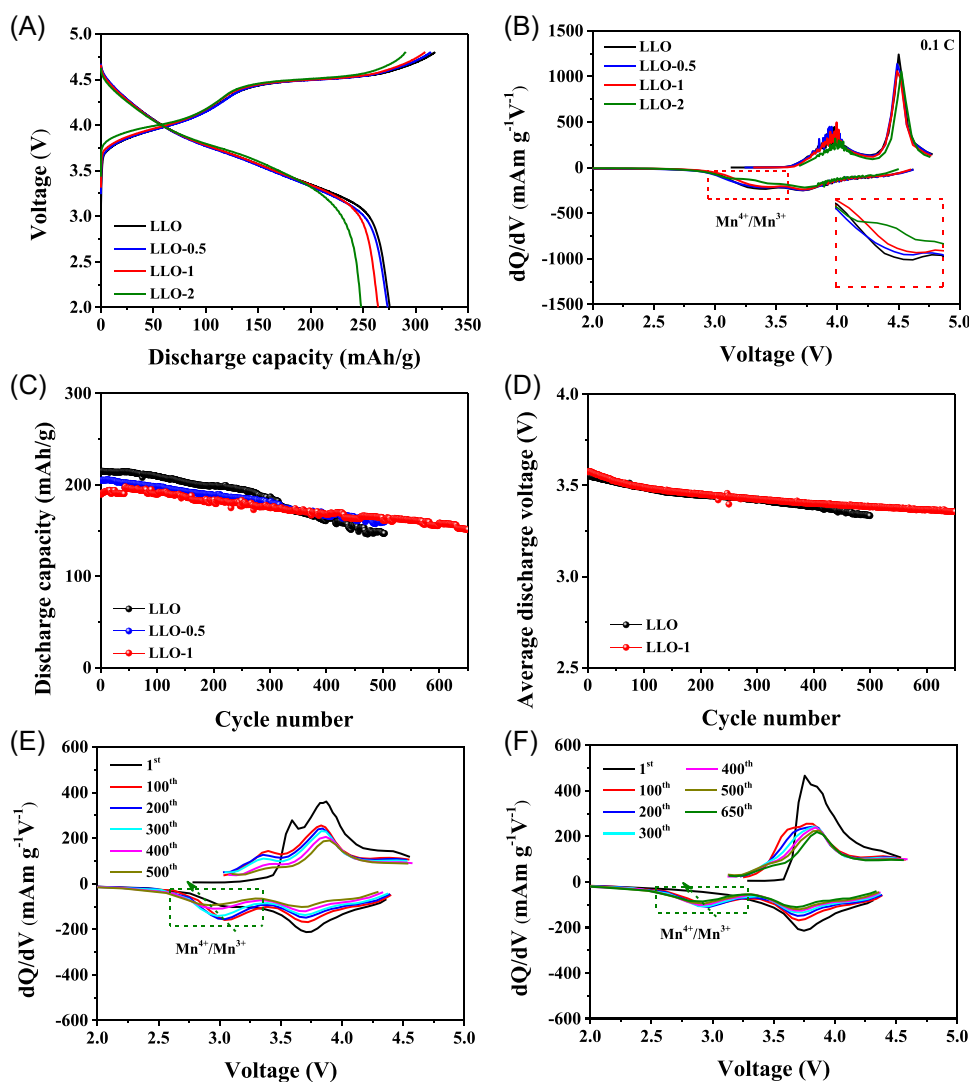
FIGURE 3 (A) Initial charge/discharge curves of lithium-rich layered oxides (LLOs), LLO-0.5, LLO-1, and LLO-2 at 0.1 C (1C = 200 mA g^{-1}). (B) The corresponding dQ/dV curves. (C, D) Cycle performance (C) and average discharge voltages (D) of LLO and LLO-1 at 1C and 25°C. (E) The dQ/dV curves of LLO (E) and LLO-1 (F) during long cycling at 1C.

significantly affect the TM redox reactions, but mainly affects the activation of the Li_2MnO_3 crystal domain and the O redox reactions. Moreover, there is little polarization or overpotential of Ta-doped LLOs at 0.1C, although slight polarizations appear at 1C (Supporting Information: Figure S6). On the other hand, the discharge capacities of LLO, LLO-0.5, LLO-1, and LLO-2 in the first cycle are 275.4, 273.3, 260.1, and 250.1 mAh g^{-1}, with the corresponding Coulombic efficiencies to be 86.4%, 86.9%, 85.2%, and 87%, respectively. In the discharge process, capacity loss mainly occurs in the low voltage region (<3.5 V).

To better understand the electrochemical effects of Ta doping on LLOs, the dQ/dV curves of LLOs in the first cycle were plotted as shown in Figure 3B. It can be observed that the intensity of the O redox peak in the charge process is weakened after Ta doping, indicating the suppression of O redox activity by the Ta dopant. Moreover, the intensity of Mn^{4+}/Mn^{3+} redox peak in the discharge process is noticeably weakened after Ta doping, suggesting the suppressed activation of the Li_2MnO_3 crystal domain. Besides, the capacity loss of LLOs is more severe at 1C (Supporting Information: Figure S6). Since LLO-2 shows noticeable polarization and severe capacity loss, it is considered that excess Ta doping (2 mol%) is not beneficial to the optimization of the performance of LLOs.

Figure 3C displays the cycling performance of LLO, LLO-0.5, and LLO-1 in the voltage range of 2.0–4.6 V at 1C. After 500 cycles, the capacity retentions of LLO, LLO-0.5, and LLO-1 are 68.4%, 77.8%, and 85.3%, respectively, suggesting that the Ta dopant can significantly improve the cycle stability of LLOs. A parallel study of LLO-1 further demonstrates the good capacity retention (85.7%) of LLO-1 within 500 cycles (Supporting Information: Figure S7). In addition, LLO-1 can maintain a capacity retention of 80.0% with consistent Coulombic efficiency even after 650 cycles (Figure 3C and Supporting Information: Figure S8), highlighting the effectiveness of Ta doping for high cycling performance LLOs.

Figure 3D presents the average voltage decay of LLO and LLO-1 during cycling at 1C. Within 650 cycles, the average voltage decay of LLO-1 is 0.34 mV cycle^{-1}, which is less than that of LLO (0.44 mV cycle^{-1}), indicating that Ta doping can suppress the discharge voltage decay. To better understand the influence of Ta doping on the discharge voltage decay during long cycling, the dQ/dV profiles in representative cycles are plotted in Figure 3E,F. It can be observed that the reduction peak of Mn^{4+}/Mn^{3+} gradually shifts to lower voltages upon cycling. The reduction Mn^{4+}/Mn^{3+} peak reflects the layered-to-spinel structure transformation, which causes continuous voltage decay.[17,47] The reduction Mn^{4+}/Mn^{3+}

peak of LLO shows a noticeable shift to lower voltage after 500 cycles. In contrast, the reduction Mn^{4+}/Mn^{3+} peak of LLO-1 maintains a stable voltage upon long cycling, indicating that Ta doping can improve the structure stability of LLOs to yield a reduced voltage decay rate.

The high-temperature performance of LLOs is also important for practical applications in LIBs. In our previous studies, it has been shown that bulk doping improves cyclic stability not only at room temperature (25°C), but also at high temperatures.[1] To evaluate the influence of Ta doping on the cycle performance of LLOs at high temperatures, LLO and LLO-1 were also tested at 50°C, as shown in Supporting Information: Figure S9. Obviously, LLO-1 delivers a higher capacity retention of 80% than that of LLO (61%) after 300 cycles. The result again proves the effectiveness of Ta doping in improving the cycle stability of LLOs.

To investigate the effect of Ta doping on the charge compensation, the chemical evolution of LLOs in the initial charge process was monitored by ex situ sXAS. The Mn, Ni, and Co L-edges of the electrodes were examined at different cut-off voltage states (Initial, C-4.05 V, C-4.4 V, C-4.5 V, and C-4.8 V, corresponding to the initial, charging to 4.05 V, 4.4 V, 4.5 V, and 4.8 V cut-off voltages, respectively). Supporting Information: Figure S10a,b shows the Mn $L_{2,3}$-edge sXAS spectra of LLO and LLO-1 at various charge states during the initial cycle, respectively. The two peaks of the Mn $L_{2,3}$-edge spectrum keep unchanged during the initial cycle, which is attributed to the inactive Mn^{4+} not participating in the charge compensation.[1,9] Meanwhile, the Mn $L_{2,3}$-edge spectrum of LLO-1 also keep unchanged during the first charge states. Supporting Information: Figure S10C,D shows that the Co^{3+} L_3-edge peak shifts to higher energy at 4.05 V and then keep unchanged. Compare with that of LLO, the Co^{3+} L_2-edge peak of LLO-1 shows a similar trend. These results indicate that Ta doping has no obvious effect on the redox of Mn and Co during the initial charge process.

Therefore, we focus on the evolutions of electronic structures of Ni and O. Figure 4A shows the Ni L_3-edge spectrum, displaying feature peaks at ~852.8 eV (L_{3-low}) and ~855.0 eV (L_{3-high}). The intensity of the L_{3-high} peak gradually increases below 4.4 V, and then gradually decreases above 4.4 V during the initial charge process, which is mainly due to the local charge exchange between Ni and O in deep delithiation states (>4.4 V).[48] The L_{3-high}/L_{3-low} ratio is shown in Supporting Information: Figure S11. The increase (<4.4 V) and decrease (>4.4 V) of the L_{3-high}/L_{3-low} ratio provide direct experimental evidence of the Ni oxidation process that takes place at low voltage states (<4.4 V) and the reduction process that takes place at high voltage states (>4.4 V).
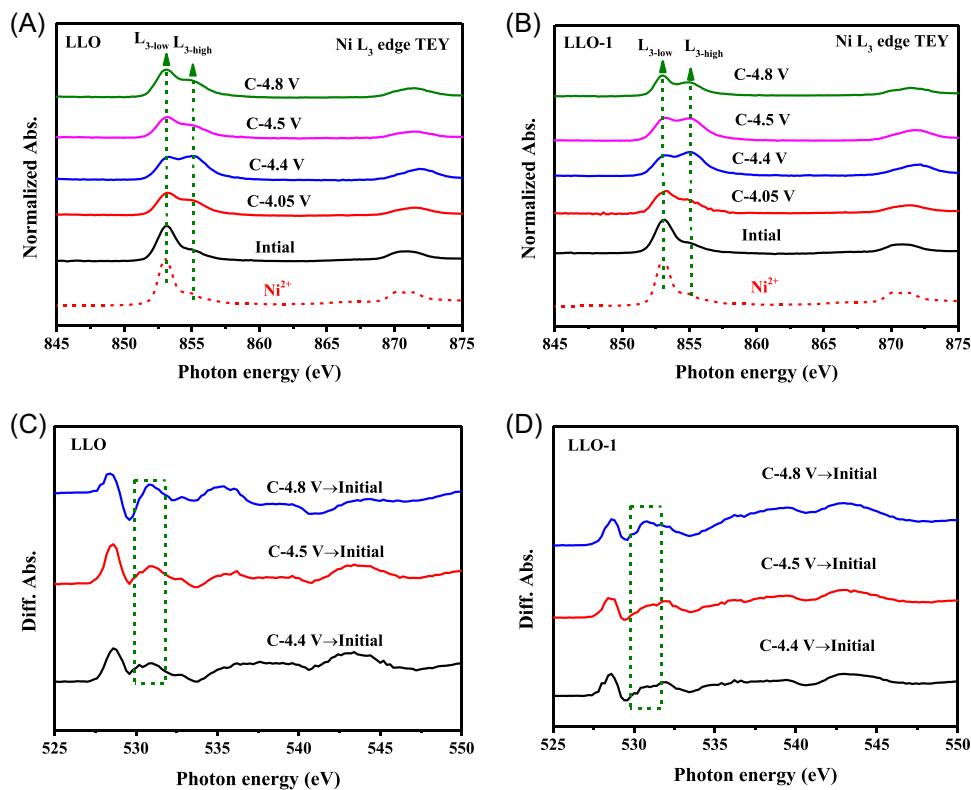
FIGURE 4 (A, B) The Ni L-edge X-ray adsorption spectroscopy (sXAS) of lithium-rich layered oxides (LLOs) (A) and LLO-1 (B) at various charge states in the first cycle in the total electron yield (TEY) modes. (C, D) The differential spectra of LLO (C) and LLO-1 (D) from the O K-edge sXAS are in Supporting Information: Figure S12.

The value of the L_{3-high}/L_{3-low} of LLO-1 is higher than that of LLO at high voltages, indicating the reduction process of Ni with a high oxidation state is suppressed. This is mainly due to the reduced local charge exchange between Ni and O at the deep delithiation state.

The activity of O in the initial charge process was also probed by sXAS. As shown in Supporting Information: Figure S12, a typical feature peak at ~530.8 eV can be observed when LLO and LLO-1 are charged at 4.8 V, which represents the characteristic peak of the anionic redox reaction of O.[49] To further explore the systematic evolution of lattice oxygen in the initial charge process, the differential O K-edge spectra of LLO and LLO-1 are displayed in Figure 4C,D, respectively. For both materials, the characteristic peak at 530.8 eV in the differential spectrum gradually increases with the increase of cut-off voltage, indicating the gradually increased activity of oxygen anionic redox. However, the intensity of this feature peak is weakened after Ta doping, which means the activity of O is suppressed after Ta doping. This result is mainly attributed to the stabilization of lattice O by the strong Ta-O and reduced Ni-O covalency.

In situ XRD was employed to study the structural evolution of LLO and LLO-1 during the initial two cycles (Figure 5). The 2D contour plot in Figure 5A shows the

evolution of the (003) peak of LLO. During the charge process below 4.4 V, the (003) peak gradually shifts to a lower diffraction angle with the increase of voltage. The downshift of the (003) peak, reflecting the increase of lattice parameter c, is ascribed to the extraction of Li^+ from the $LiTMO_2$ crystal domain (Figure 5C) and the accompanying increase of electrostatic repulsion between neighboring O layers. During further charge process between 4.4 and 4.8 V, corresponding to the activation of Li_2MnO_3 crystal domain, the (003) peak begins to shift to higher diffraction angles, suggesting the decrease of parameter c. In this process, the irreversible release of O and the migration of TM can reduce the electrostatic repulsive force between neighboring O layers, resulting in the gradual reduction of layer spacing and lattice parameter c.

Compared with that of LLO, the (003) peak of LLO-1 shows a similar evolution trend during the initial charge process below 4.4 V (Figure 5B). However, between 4.4 and 4.8 V, the shift of (003) peak towards higher diffraction angles is weakened, which suggests the increased stability of LLO after Ta doping. We compare the volume change ($\Delta V = V_{C-4.8} - V_{D-2.0}$) from the 4.8 V charge state ($V_{C-4.8}$) to the 2.0 V discharge state ($V_{D-2.0}$). LLO displays a large volume change of 3.97 Å^3 and 4.22 Å^3 in the first and second cycles, respectively
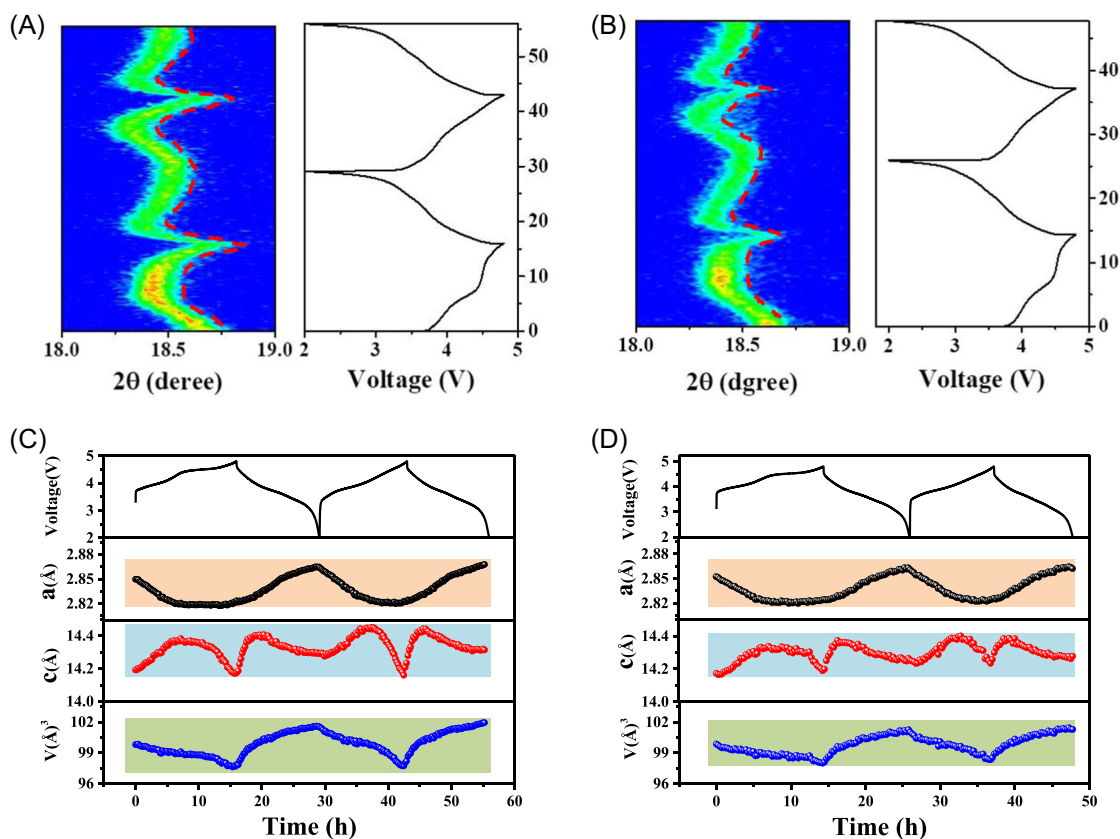
FIGURE 5 In situ X-ray powder diffraction (XRD) studies of lithium-rich layered oxides (LLOs) and LLO-1 during the initial two cycles at 0.1 C. (A, B) The 2D contour plot of (003) peaks of LLO (A) and LLO-1 (B). (C, D) The variation of lattice parameters *a*, *c*, and *V* of LLO (C) and LLO-1 (D).

(Figure 5C). In contrast, LLO-1 displays reduced volume changes of 3.27 and 3.3 $Å^3$ in the first and second cycles, respectively (Figure 5D). It clearly indicates that the Ta doping strategy can improve the structural stability of LLOs.

For the sake of revealing the influence of Ta doping on the structural stability of LLOs, XRD was carried out to examine the structures of LLO and LLO-1 after 500 cycles. Figure 6A–C shows the XRD patterns of cycled LLO and LLO-1. In the LLO case, although the main characteristic peaks (such as [003], [101], and [104]) of layered structures are maintained after 500 cycles, new peaks clearly appear at 19° and 36.4° in the XRD pattern, which belongs to the spinel-like structures.[50] In contrast, in the LLO-1 case, the characteristic peaks of spinel-like structures can hardly be observed in the XRD pattern. Based on the refined XRD patterns as shown in Supporting Information: Figure S13, the fractions of the spinel-like structures in LLO and LLO-1 after 500 cycles are 17.24% and 7.9%, respectively.

The atomic structures of the LLO and LLO-1 electrodes after 500 cycles were further studied by HAADF/ABF-STEM imaging. As shown in Figure 6D

and Supporting Information: Figure S14a, two legible sets of lattice fringes in the surface region of the cycled LLO can be clearly identified. The outermost region with a thickness of ~7 nm is the spinel structure, which can be further identified by the corresponding FFT pattern in the inset of Figure 6D. Figure 6F shows the selected region A in Figure 6D and region C in Supporting Information: Figure S14a, where the spinel frameworks are clearly observed. However, in the cycled LLO-1 case (Figure 6E,G, and Supporting Information: Figure S14b), although the outmost spinel layer still exists, the thickness is only around 3 nm, in line with the XRD results. It indicates that Ta doping can suppress the layer-to-spinel transformation of LLOs during long cycles.

Since the electrochemical behavior of O plays a key role to determine the stability of LLOs, the behaviors of lattice O in LLO and LLO-1 were further investigated. In situ differential electrochemical mass spectroscopy (DEMS) was used to directly monitor the gas evolution phenomena of both LLO and LLO-1 during the initial cycle. As shown in Figure 7A, the release of O_2 is detectable between 4.6 and 4.8 V for LLO/Li cells. However, the signal of O_2 is very weak and only starts
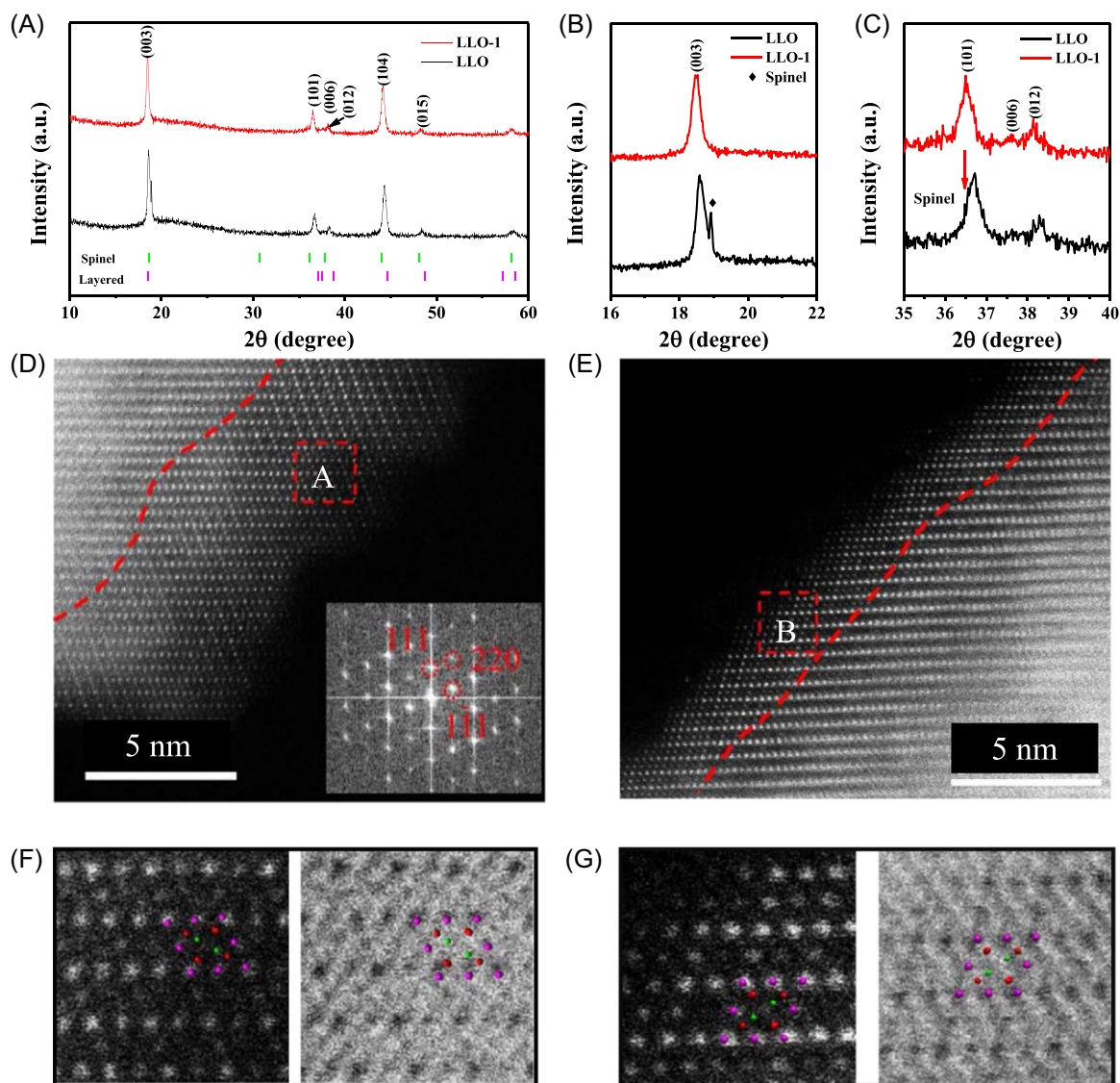
FIGURE 6 (A) X-ray powder diffraction (XRD) patterns of lithium-rich layered oxides (LLOs) and LLO-1 electrodes after 500 cycles. (B, C) The enlarged views of (003) (B) and (101) (C) peaks. (D, E) HAADF-STEM images of LLO (D) and LLO-1 (E) after 500 cycles. (F, G) The enlarged HAADF/ABF-STEM images of LLO (F) and LLO-1 (G) from regions A in (D) and B in (E), respectively. The green, purple, and red disks in these crystal-structure images stand for the Li elements, TM elements, and O elements, respectively.

from 4.75 V for LLO-1 (Figure 7B). For both LLO and LLO-1, the generation of CO_2 signals starts at ~4.2 V, which may be resulted from the decomposition of trace amounts of carbonate residual (such as Li_2CO_3) at the surface of LLOs. Then, clearly, peaks appear at 4.6 V, which can be attributed to the electrochemical oxidation of carbonate molecules by the attack of superoxo species.[51–53] Although CO_2 releases can be detectable in the two cathode materials, the total amount of CO_2 release in LLO-1/Li cell is less than that of LLO/Li cell, indicating the electrochemical decomposition is partly inhibited in LLO-1/Li cell. Therefore, both the O_2 and CO_2 releases indicate that

Ta doping can stabilize the lattice O by the strong Ta-O bond and reduced Ni-O covalency to inhibit the O_2 release and oxidation of electrolyte solvents.

First-principles calculations were further performed to understand the effect of Ta on the lattice O. Since the activity of O is related to Li_2MnO_3 in LLOs, Li_2MnO_3 and Ta-doped Li_2MnO_3 model structures are employed in the calculation, as depicted in Supporting Information: Figure S15. The formation energy $\Delta E(Vo)$ of oxygen vacancy (Vo) was calculated by the below equation:

$$\Delta E(Vo) = 0.5E(O_2) + E(Vo) - E(p), \quad (1)$$
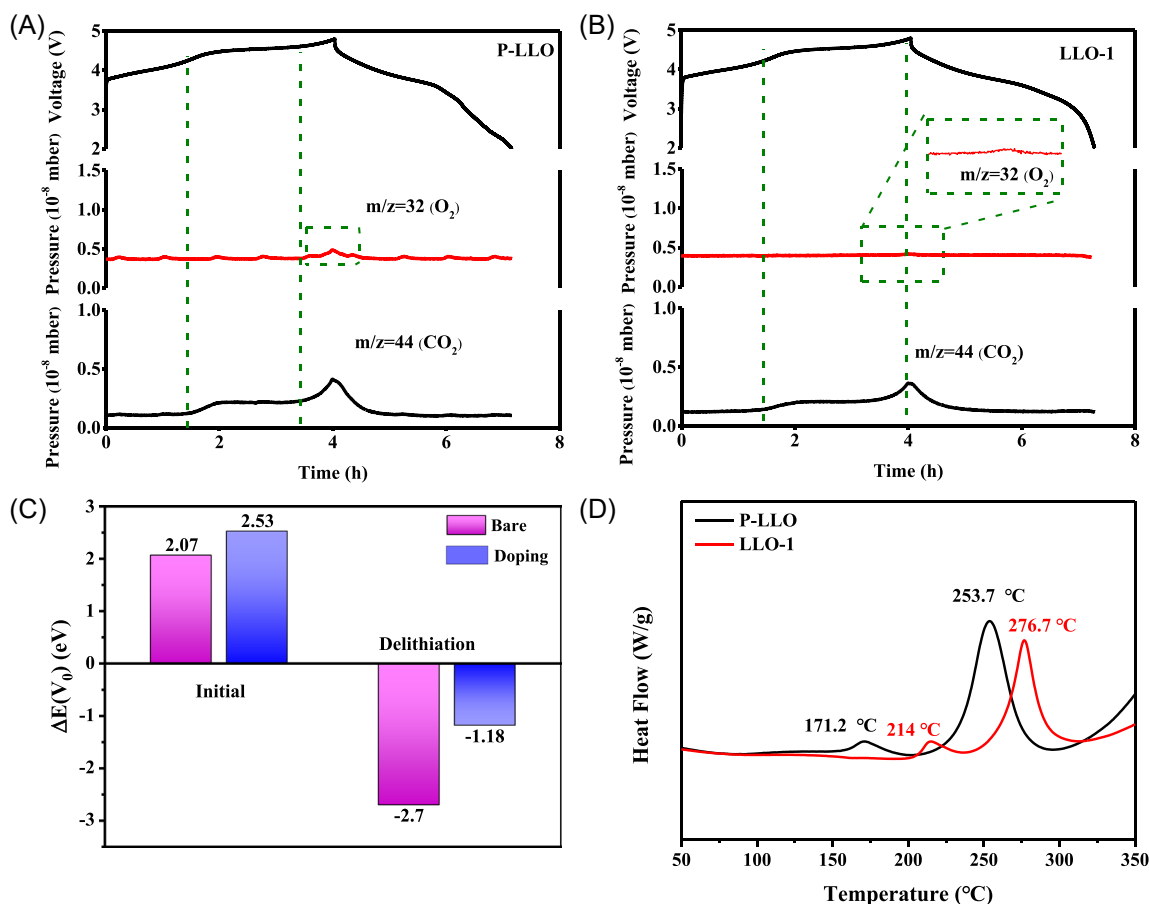
FIGURE 7 The evolutions of O_2 and CO_2 gases of (A) lithium-rich layered oxides (LLOs) and (B) LLO-1. (C) The formation energies of oxygen vacancies in Li_2MnO_3 and Ta-doped Li_2MnO_3. (D) differential scanning calorimetry (DSC) curves of LLO and LLO-1 after being charged to 4.8 V.

where E(p), E(O_2), E(Vo) are the energy of the pristine structure, the O_2 molecule, and the structure with oxygen vacancy, respectively. As shown in Figure 7, the ΔE(Vo) values of pristine and Ta-doped Li_2MnO_3 are 2.07 and 2.53 eV, while those of pristine and Ta-doped Li_2MnO_3 at the charge state are −2.7 and −1.18 eV, respectively. It suggests that the release of O in LLOs to form O vacancy can be suppressed by Ta doping.

The thermal stability of LLOs reflects the generation of heat, which directly affects the safety of LIBs.[8,19] To verify the effect of Ta doping on thermal stability, LLO and LLO-1 charged to 4.8 V were analyzed by DSC, as shown in Figure 7D. The exothermic peaks of LLO are located at 171.2°C and 253.6°C with a specific heat release of 453.97 J g^{-1}. In contrast, the exothermic peaks of LLO-1 are raised to 214°C and 276.7°C, respectively. Meanwhile, LLO-1 delivers a lower heat release of 304.2 J g^{-1}, indicating improved thermal stability after Ta doping. Therefore, Ta doping can not only improve the cycle stability, but also the thermal stability of LLOs,

which presents a useful strategy for the optimization of LLOs for applications.

4 | CONCLUSIONS

In summary, a Ta doping strategy has been proposed to stabilize LLOs for enhanced electrochemical performance. Based on a series of characterizations, it is demonstrated that the Ta^{5+} dopant can expand the interlayer spacing owing to its large radius and change the electronic state of Ni owing to the rebalance of charge. The Ta-doped LLO with optimal amount delivers greatly enhanced long-cycle performance (80% capacity retention within 650 cycles) and small voltage decay (0.34 mV cycle^{-1}). Based on a series of ex situ and in situ characterizations, the enhancement of cycle performance and suppression of voltage decay of the Ta-doped LLOs can be attributed to the following factors. (1) The strong Ta-O bonds stabilize the lattice oxygen and suppress the gas release (O_2 and CO_2). (2) The reduced covalency of

the Ni-O bond suppresses the activation of lattice O. (3) The Ta dopant can effectively maintain the stability of crystal structure, and hinder the layer-to-spinel degradation. These results provide a rational strategy and basis for the design of high-performance LLOs.

CONFLICT OF INTEREST

The authors declare no conflict of interest.

DATA AVAILABILITY STATEMENT

The data that support the findings of this study are available from the corresponding author upon reasonable request.

ORCID

Haijun Yu http://orcid.org/0000-0003-0204-9943

REFERENCES

1. Wang E, Xiao D, Wu T, et al. Al/Ti synergistic doping enhanced cycle stability of Li-rich layered oxides. *Adv Funct Mater*. 2022;32:2201744.
2. Zhang J, Zhang Q, Wong D, et al. Addressing voltage decay in Li-rich cathodes by broadening the gap between metallic and anionic bands. *Nat Commun*. 2021;12:3071.
3. Clément RJ, Lun Z, Ceder G. Cation-disordered rocksalt transition metal oxides and oxyfluorides for high energy lithium-ion cathodes. *Energy Environ Sci*. 2020;13:345-373.
4. Zhang X, Wang B, Zhao S, Li H, Yu H. Oxygen anionic redox activated high-energy cathodes: status and prospects. *eTransportation*. 2021;8:100118.
5. Wang E, Zhao Y, Xiao D, et al. Composite nanostructure construction on the grain surface of Li-rich layered oxides. *Adv Mater*. 2020;32:1906070.
6. Yu H, Zhou H. High-energy cathode materials (Li_2MnO_3-$LiMO_2$) for lithium-ion batteries. *J Phys Chem Lett*. 2013;4: 1268-1280.
7. Oishi M, Yamanaka K, Watanabe I, et al. Direct observation of reversible oxygen anion redox reaction in Li-rich manganese oxide, Li_2MnO_3, studied by soft X-ray absorption spectroscopy. *J Mater Chem A*. 2016;4:9293-9302.
8. Hu E, Yu X, Lin R, et al. Evolution of redox couples in Li- and Mn-rich cathode materials and mitigation of voltage fade by reducing oxygen release. *Nat Energy*. 2018;3:690-698.
9. Luo K, Roberts MR, Hao R, et al. Charge-compensation in 3d-transition-metal-oxide intercalation cathodes through the generation of localized electron holes on oxygen. *Nat Chem*. 2016;8:684-691.
10. Yu H, So YG, Kuwabara A, et al. Crystalline grain interior configuration affects lithium migration kinetics in Li-rich layered oxide. *Nano Lett*. 2016;16:2907-2915.
11. Yang Y, Zhang Z, Liu S, et al. Cation configuration in transition-metal layered oxides. *Matter*. 2022;5:3869-3882.
12. Yu H, So YG, Ren Y, et al. Temperature-sensitive structure evolution of lithium-manganese-rich layered oxides for lithium-ion batteries. *J Am Chem Soc*. 2018;140:15279-15289.
13. Meng J, Xu L, Ma Q, et al. Modulating crystal and interfacial properties by W-gradient doping for highly stable and long life Li-rich layered cathodes. *Adv Funct Mater*. 2022;32:2113013.
14. Xu C, Li J, Sun J, Zhang W, Ji B. Li-rich layered oxide single crystal with Na doping as a high-performance cathode for Li ion batteries. *J Alloys Compd*. 2022;895:162613.
15. Fu C, Meng L, Wang J, et al. Bonding the terminal isocyanate-related functional group to the surface manganese ions to enhance Li-rich cathode's cycling stability. *ACS Appl Mater Interfaces*. 2021;13:17565-17576.
16. Li Q, Zhou D, Zhang L, et al. Tuning anionic redox activity and reversibility for a high-capacity Li-rich Mn-based oxide cathode via an integrated strategy. *Adv Funct Mater*. 2019;29:1806706.
17. Zhang XD, Shi JL, Liang JY, et al. Suppressing surface lattice oxygen release of Li-rich cathode materials via heterostructured spinel $Li_4Mn_5O_{12}$ coating. *Adv Mater*. 2018;30:1801751.
18. Ju X, Hou X, Beuse T, et al. Tailoring of gradient particles of Li-rich layered cathodes with mitigated voltage decay for lithium-ion batteries. *ACS Appl Mater Interfaces*. 2020;12: 43596-43604.
19. Wu T, Liu X, Zhang X, et al. Full concentration gradient-tailored Li-rich layered oxides for high-energy lithium-ion batteries. *Adv Mater*. 2021;33:2001358.
20. Kong D, Hu J, Chen Z, et al. Ti-Gradient doping to stabilize layered surface structure for high performance high-Ni oxide cathode of Li-Ion battery. *Adv Energy Mater*. 2019;9:1901756.
21. Li Z, Li Y, Zhang M, et al. Modifying Li@Mn6 superstructure units by Al substitution to enhance the long-cycle performance of co-free Li-rich cathode. *Adv Energy Mater*. 2021; 11:2101962.
22. Feng Z, Song H, Li Y, Lyu Y, Xiao D, Guo B. Adjusting oxygen redox reaction and structural stability of Li- and Mn-rich cathodes by Zr-Ti dual-doping. *ACS Appl Mater Interfaces*. 2022;14:5308-5317.
23. Yang J, Chen Y, Li Y, et al. Encouraging voltage stability upon long cycling of Li-rich Mn-based cathode materials by Ta-Mo dual doping. *ACS Appl Mater Interfaces*. 2021;13:25981-25992.
24. Wang L, Shi JL, Su H, et al. Composite-structure material design for high-energy lithium storage. *Small*. 2018; 14:1800887.

25. Bian X, Fu Q, Pang Q, et al. Multi-functional surface engineering for Li-excess layered cathode material targeting excellent electrochemical and thermal safety properties. *ACS Appl Mater Interfaces*. 2016;8:3308-3318.

26. He Z, Wang Z, Huang Z, Chen H, Li X, Guo H. A novel architecture designed for lithium rich layered Li[Li$_{0.2}$Mn$_{0.54}$Ni$_{0.13}$Co$_{0.13}$]O$_2$ oxides for lithium-ion batteries. *J Mater Chem A*. 2015; A3(32):16817-16823.

27. Chen H, He Z, Huang Z, Song L, Shen C, Liu J. The effects of multifunctional coating on Li-rich cathode material with Hollow spherical structure for Li ion battery. *Ceram Int*. 2017;43(12):8616-8624.

28. Chen H, Hu Q, Huang Z, et al. Synthesis and electro-chemical study of Zr-doped Li[Li$_{0.2}$Mn$_{0.54}$Ni$_{0.13}$Co$_{0.13}$]O$_2$ as cathode material for Li-ion battery. *Ceram Int*. 2016; 42(1):263-269.

29. Zhao J, Liang Y, Zhang X, et al. In situ construction of uniform and robust cathode–electrolyte interphase for Li-rich layered oxides. *Adv Funct Mater*. 2020;31:2009192.

30. Zhang S, Gu H, Pan H, et al. A novel strategy to suppress capacity and voltage fading of Li-and Mn-rich layered oxide cathode material for lithium-ion batteries. *Adv Energy Mater*. 2016;7:1601066.

31. Yang J, Li P, Zhong F, et al. Suppressing voltage fading of Li-rich oxide cathode via building a well-protected and partially-protonated surface by polyacrylic acid binder for cycle-stable Li-ion batteries. *Adv Energy Mater*. 2020; 10:1904264.

32. Liu S, Liu Z, Shen X, et al. Surface doping to enhance structural integrity and performance of Li-rich layered oxide. *Adv Energy Mater*. 2018;8:1802105.

33. Wu F, Kim, G-T, Kuenzel M, et al. Elucidating the effect of iron doping on the electrochemical performance of cobalt-free lithium-rich layered cathode materials. *Adv Energy Mater*. 2019;9:1902445.

34. Tang W, Duan J, Xie J, Qian Y, Li J, Zhang Y. Dual-site doping strategy for enhancing the structural stability of lithium-rich layered oxides. *ACS Appl Mater Interfaces*. 2021;13:16407-16417.

35. He W, Guo W, Wu H, et al. Challenges and recent advances in high capacity Li-rich cathode materials for high energy density lithium-ion batteries. *Adv Mater*. 2021;33:2005937.

36. Gao Y, Wang X, Ma J, Wang Z, Chen L. Selecting substituent elements for Li-rich Mn-based cathode materials by density functional theory (DFT) calculations. *Chem Mater*. 2015;27: 3456-3461.

37. Huang W, Li W, Wang L, et al. Structure and charge regulation strategy enabling superior cyclability for Ni-rich layered cathode materials. *Small*. 2021;17:2104282.

38. Kim U-H, Park G-T, Son B-K, et al. Heuristic solution for achieving long-term cycle stability for Ni-rich layered cathodes at full depth of discharge. *Nat Energy*. 2020;5: 860-869.

39. Sun HH, Kim UH, Park JH, et al. Transition metal-doped Ni-rich layered cathode materials for durable Li-ion batteries. *Nat Commun*. 2021;12:6552.

40. House RA, Marie J-J, Pérez-Osorio MA, Rees GJ, Boivin E, Bruce PG. The role of O$_2$ in O-redox cathodes for Li-ion batteries. *Nat Energy*. 2021;6:781-789.

41. Kim SY, Park CS, Hosseini S, Lampert J, Kim YJ, Nazar LF. Inhibiting oxygen release from Li-rich, Mn-rich layered oxides at the surface with a solution processable oxygen scavenger polymer. *Adv Energy Mater*. 2021;11:2100552.

42. Jamil S, Yu R, Wang Q, et al. Enhanced cycling stability of nickel-rich layered oxide by tantalum doping. *J Power Sources*. 2020;473:228597.

43. Liu J, Banis MN, Li X, et al. Atomic layer deposition of lithium tantalate solid-state electrolytes. *J Phys Chem C*. 2013;117: 20260-20267.

44. Li N, Sallis S, Papp JK, et al. Unraveling the cationic and anionic redox reactions in a conventional layered oxide cathode. *ACS Energy Lett*. 2019;4:2836-2842.

45. Steiner JD, Cheng H, Walsh J, et al. Targeted surface doping with reversible local environment improves oxygen stability at the electrochemical interfaces of nickel-rich cathode materials. *ACS Appl Mater Interfaces*. 2019;11:37885-37891.

46. Li B, Yan H, Ma J, et al. Manipulating the electronic structure of Li-rich manganese-based oxide using polyanions: towards better electrochemical performance. *Adv Funct Mater*. 2014; 24:5112-5118.

47. Jiang W, Zhang C, Feng Y, et al. Achieving high structure and voltage stability in cobalt-free Li-rich layered oxide cathodes via selective dual-cation doping. *Energy Storage Mater*. 2020;32:37-45.

48. Zhang Z, Zhao S, Wang B, Yu H. Local redox reaction of high valence manganese in Li$_2$MnO$_3$-based lithium battery cathodes. *Cell Rep Phys Sci*. 2020;1:100061.

49. Liu Z, Liu S, Yang L, et al. Feasibility to improve the stability of lithium-rich layered oxides by surface doping. *ACS Appl Mater Interfaces*. 2022;14(16):18353-18359.

50. Sun YK, Lee MJ, Yoon CS, Hassoun J, Amine K, Scrosati B. The role of AlF$_3$ coatings in improving electrochemical cycling of Li-enriched nickel-manganese oxide electrodes for Li-ion batteries. *Adv Mater*. 2012;24:1192-1196.

51. Qiu B, Zhang M, Wu L, et al. Gas-solid interfacial modification of oxygen activity in layered oxide cathodes for lithium-ion batteries. *Nat Commun*. 2016;7:12108.

52. Sun J, Sheng C, Cao X, et al. Restraining oxygen release and suppressing structure distortion in single-crystal Li-rich layered cathode materials. *Adv Funct Mater*. 2021;32:2110295.

53. Gao H, Zeng X, Hu Y, et al. Modifying the surface of a high-voltage lithium-ion cathode. *ACS Appl Energy Mater*. 2018;1: 2254-2260.

SUPPORTING INFORMATION

Additional supporting information can be found online in the Supporting Information section at the end of this article.